X-ray Far-field Ptychotomography

Venkata Sree Charan Kuppili

Upgrade from MPhil Degree to PhD Degree
May 2016

Supervisor
Dr. Pierre Thibault

University College London
Department of Physics and Astronomy
Gower Street WC1E 6BT

Declaration

I, Venkata Sree Charan Kuppili confirm that the work presented in this thesis is my own. Where information has been derived from other sources, I confirm that this has been indicated in the thesis.

(London,May 2016.)

Abstract

X-ray far field ptychography has gained prominence in recent times as a must go technique for imaging nano-structures and nano-materials. Ptychography can give high resolution complex transmission maps of the samples under study, it achieves this by collecting x-ray diffraction patterns at various scan points on the object which are later processed through non-linear iterative search algorithms to uncover the embedded information.It has been recently demonstrated that this technique can be applied to obtain high resolution, high contrast complex transmission maps in both 2 and 3 dimensions. It would be possible to combine fluorescence data from the sample thus throwing insights into chemical and structural information of the sample at one go. In principle the technique should also be able to image fast dynamic stochastic processes of this physical world. This report discusses the theoretical and experimental details of x-ray far field ptychography, along with future plans and possible directions in which this technique can be improved and applied.

Table of Contents

List of Figures

1 Introduction

Imaging can play a very big role in shedding light on many unknown mysteries of the physical world. Ability to image at better resolutions and higher contrasts might improve our chances of understanding complex scientific problems ranging from structure-property relationships to cutting edge diagnosis techniques (Dierolf et al., 2010; da Silva et al., 2015; Elleaume et al., 2002). In-situ imaging of processes like behaviour of matter under extreme physical conditions might give us more insights into phenomenon that occurred far in time and space (Bø Fløystad et al., 2015; Mezouar et al., 2005; Pfeifer et al., 2006). Better understanding of commonly occurring natural phenomenon like corrosion, fracture mechanics and phase transitions might lead to interesting technological and engineering applications.

From the onset of discovery of x-rays in 1895, incidentally with an image of his wife's hand, X-rays have found numerous applications in diverse scientific areas ranging from protein crystallography to energy research. While techniques such as x-ray crystallography give a detailed account of periodic arrangement of atoms in the matter, spectroscopic techniques such as XANES and EXAFS give information about chemical composition and chemical environment. X-ray imaging which was largely the domain of medical imaging community, gained traction with applications of computational tomography in explaining macroscopic and microscopic phenomenon (Schenk et al., 2005; Walker et al., 2014). Inroads into imaging nanostructures were made with the advent of scanning transmission x-ray microscopy (**STXM**) (Horowitz et al., 1972) ,**STXM** techniques with resolution limited by focal spot size progressed with progress of nanofocussing techniques. Collecting fluorescence spectra simultaneously with transmission images enabled simultaneous structural and chemical imaging (Ortega et al., 2007). **STXM** techniques suffered with two main drawbacks firstly, the resolution is determined by the focal spot hence making it impractical to image large fields of view and secondly, the technique could not give phase contrast. In the hard x-ray regime phase contrast dominates the absorption contrast and the difference can be a few orders of magnitude for sufficiently small wavelengths.

Lensless imaging was envisioned as a way to overcome inefficient x-ray lenses and limitations of STXM techniques along with gaining on the phase contrast. Advancements in lensless imaging techniques took root with (Sayre, 1952) who opinionated that solving the phase problem becomes viable if the crystal diffraction pattern is sufficiently over sampled. While (Gerchberg, R W and Saxton, W O, 1972) and (Fienup, 1978) should be accredited with developing iterative algorithms for phase retrieval, (Miao

Figure 1.1: X-ray image of Anna Bertha's hand, Source: wikipedia.org

et al., 1999) should be acknowledged for the first ever experimental demonstration of x-ray lensless imaging. Ptychographic imaging employing iterative algorithms was first demonstrated by (Faulkner and Rodenburg, 2004) meanwhile (Thibault et al., 2009) demonstrated the robust methodology of retrieving object's transmission function along with probe's illumination function by employing difference map algorithm. The rest of the report will focus on the theoretical, algorithmic and experimental details of ptychography.

2 Theory

2.1 Ptychography

Ptychography combines standard STXM techniques with coherent diffractive imaging (**CDI**) producing high contrast, high resolution transmission maps of the sample (Faulkner and Rodenburg, 2004). Typically the sample is scanned perpendicular to this axis of propagation of a coherent x-ray beam, collecting diffraction images at each of these scanned point. The diffraction patterns are then processed through iterative reconstruction algorithms (Rodenburg et al., 2007; Thibault et al., 2009) resulting in a complex transmission map of the object. As an added advantage, the illumination function of the probe can also be reconstructed along with the transmission map of the object. This in turn can be used to diagnose x-ray beam and x-ray beam-optics. (Kewish et al., 2010b,a).

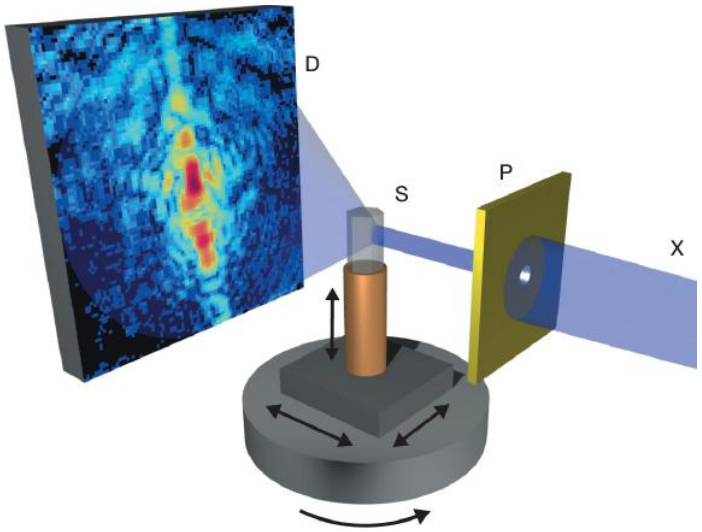

Figure 2.1: Ptychographic experimental schematic (Dierolf et al., 2010). **D** corresponds to array detector, **S** is the sample, **P** corresponds to focusing optics and **X** corresponds to x-rays

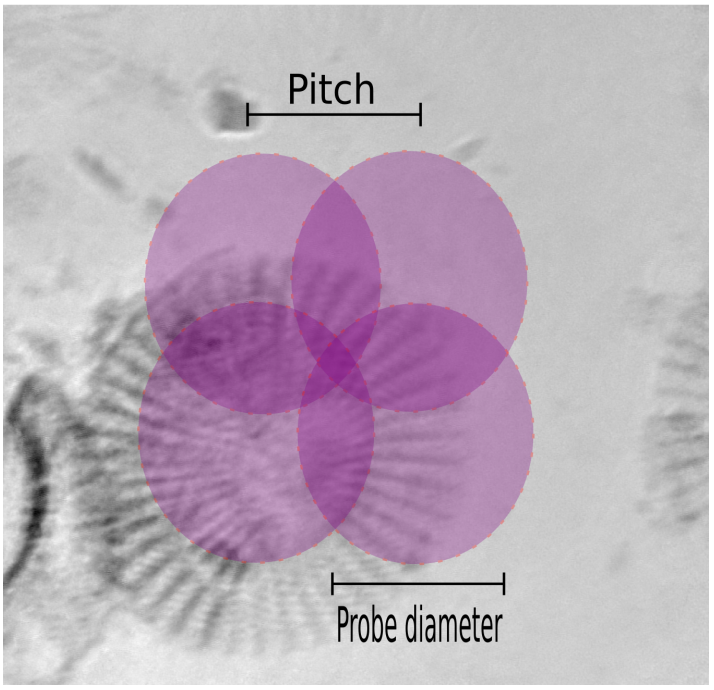

Figure 2.2: Figure illustrating overlap criterion

2.1.1 General aspects of ptychography

Several parameters, illustrated in the figures 2.1 and 2.2 play a key role in deciding the feasibility and quality of the reconstructed transmission map. Sample to detector distance plays a part in determining the obtainable resolution (Thibault et al., 2009; Thibault, 2008; van der Veen, 2004). Combined with probe size it determines whether the interaction falls under the near field or far field regime. Probe size by itself determines the speckle size, poor speckle visibility leads to in-feasibility of the reconstructions. (Guizar-Sicairos et al., 2012) demonstrated that the resolution of a ptychographic reconstruction can be enhanced by tailoring the frequency spectrum of illumination function of the probe. Unlike CDI where obtaining phase information is solely dependent on the oversampling condition in the Fourier space, ptychography takes into consideration a combination of both oversampling in the Fourier space and overlap in the real space to attain enough redundancy for the reconstruction to be feasible (Thibault, 2008; Batey et al., 2014). (Edo et al., 2013) has introduced a quantity called fundamental ptychographic sampling to explain the interplay of these two parameters. The information of positions of points where diffraction patters are collected is crucial in ptychography, error in obtaining this information might lead to blurring and loss of resolution (Edo et al., 2013).

2.2 Phase Retrieval and Phase retrieval algorithms

Reconstructive algorithms employed by ptychography ranges from ordinary error minimisation methods to non linear iterative algorithms like difference map (Fienup, 1982; Yang et al., 2011; Thibault, 2007). Originally it was proposed that ptychographic imaging can be carried through Wigner deconvolution methods (McCallum and Rodenburg, 1992; Chapman, 1997) however this approach was deemed impractical as data collected would be too large. Non linear iterative algorithms such as hybrid input output methods and difference mapping algorithm (Elser, 2002; Fienup, 1982; Luke, 2005) proved both robust and consistent. Further details on these algorithms would be discussed in the following sections.

2.2.1 Difference map algorithm

Difference Map algorithm belongs to a general class of phase-retrieval algorithms with wider applications in search based problems of combinatorial character (Elser et al., 2007). The algorithm tries to find a unique solution for variables satisfying multiple constraint sets. The algorithm accomplishes this by employing projectors that map the variables to their respective constraint sets. The projectors map the variables iteratively and non-linearly till an agreeable solution is reached, (Elser et al., 2007) showed that difference map can tackle problems ranging from protein folding to sudoku.

Difference map algorithm can be applied to ptychographic phase-retrieval problem by modelling the exit wave leaving the object as a product between probe's illumination function and object's transmission function, this also doubles as one of the constraint sets (2.1). The ptychographic data set hence becomes (2.2) where $\mathscr{F}$ is the Fourier transform.

$$\psi_j(\boldsymbol{r}) = O(\boldsymbol{r})P(\boldsymbol{r} - \boldsymbol{r}_j), \tag{2.1}$$

$$I_j = |\mathscr{F}\psi_j|^2 . \tag{2.2}$$

This formulation allows us to choose a high-dimensional euclidean space containing both the constraint sets as our search space. This search space in which the iterations are carried out is the direct product of each individual exit wave. Once this framework is formulated, all that remains is to define our constraint sets. First one, the Fourier constraint restricts the data set to agree with the measured intensities. The projection corresponding to this constraint, denoted by P_F involves replacing the magnitudes of the Fourier transforms of the individual exit waves with $\sqrt{I_j}$ while keeping the original phases unchanged (2.3) here Ψ is the state vector of the high dimensional euclidean space $\Psi = (\psi_1, \psi_2, ...\psi_N)$.

$$\Pi_F(\Psi) : \psi_j \to \psi_j^F = \mathrm{P_F}\,(\psi_j). \tag{2.3}$$

The second projection is the overlap projection which boils down to minimisation of $||\Psi - \Psi^o||^2$ subjected to the overlap constraint (2.1) thus the corresponding projection Π_O (2.4) boils down to finding $\hat{P}$,$\hat{O}$ that minimises (2.5). Though (2.5) can be minimised in multiple ways (Thibault et al., 2009) the most straightforward way would be to set the derivative of $||\Psi - \Psi^o||^2$ with respect to $\hat{P}$,$\hat{O}$ to zero. This gives rise to system of equations (2.6). Difference Map (2.7), is applied on to the ptychographic data with the aforementioned projectors finding a solution satisfying both the Fourier and the overlap constraints.

$$\Pi_O(\Psi) : \psi_j \rightarrow \psi_j^O = \hat{O}(\boldsymbol{r})\hat{P}(\boldsymbol{r}), \tag{2.4}$$

$$||\Psi - \Psi^o||^2 = \sum_j \sum_{\boldsymbol{r}} |\psi_j(\boldsymbol{r}) - \hat{O}(\boldsymbol{r})\hat{P}(\boldsymbol{r} - \boldsymbol{r}_j)|^2, \tag{2.5}$$

$$\begin{aligned} \hat{P}(\boldsymbol{r}) &= \frac{\sum_j \hat{O}^*(\boldsymbol{r} + \boldsymbol{r}_j)\psi_j(\boldsymbol{r})}{\sum_j |\hat{O}(\boldsymbol{r} + \boldsymbol{r}_j)|^2}, \\ \hat{O}(\boldsymbol{r}) &= \frac{\sum_j \hat{P}^*(\boldsymbol{r} - \boldsymbol{r}_j)\psi_j(\boldsymbol{r})}{\sum_j |\hat{P}(\boldsymbol{r} - \boldsymbol{r}_j)|^2}, \end{aligned} \tag{2.6}$$

$$\Psi_{n+1} = \Psi_n + \Pi_F \left[2\Pi_O \left(\Psi_n\right) - \Psi_n\right] - \Pi_O \left(\Psi_n\right). \tag{2.7}$$

2.2.2 Maximum likelihood methods

In the presence of no noise, the aforementioned formulation becomes ill-posed and an unique solution can longer be guaranteed. Maximum likelihood method is one of the most widely used technique in the experimental sciences community to deal with the problem of noisy data. It has found wide use in the field of crystallography as a way of further refining atomic parameters once the initial atomic model has been finalised. (Thibault and Guizar-Sicairos, 2012) has presented an in-depth analysis of maximum likelihood methods as an additional step to improve resolution and decrease the noise of reconstructions, once a probable initial solution is reached by the difference map algorithm.

$$p(n_{j\boldsymbol{q}}|P_{\boldsymbol{r}}, O_{\boldsymbol{r}}) = \frac{(I_{j\boldsymbol{q}})^{n_{j\boldsymbol{q}}}}{n_{j\boldsymbol{q}}!} e^{-Ij\boldsymbol{q}}. \tag{2.8}$$

The probability of measuring $n_{j\boldsymbol{q}}$ photons assuming Poisson noise distribution model is (2.8) where $I_{j\boldsymbol{q}}$ is the intensity at the position $\boldsymbol{q}$ of the far-field plane. The negative log-likelihood function therefore becomes (2.9) here $w_{j\boldsymbol{q}}$ is a mask function that forces bad pixels to zero. This is needed, as sum over $\boldsymbol{q}$ must include only valid measurements.

$$\begin{aligned}\mathscr{L} &= -log \prod_{j} \prod_{\boldsymbol{q}} p(n_{j\boldsymbol{q}}|P_{\boldsymbol{r}}, O_{\boldsymbol{r}}) \\ &= -\sum_{j} \sum_{\boldsymbol{q}} w_{j\boldsymbol{q}}[n_{j\boldsymbol{q}} log(I_{j\boldsymbol{q}}) - I_{j\boldsymbol{q}} - log(n_{j\boldsymbol{q}}!)].\end{aligned} \tag{2.9}$$

In order to minimise the negative log-likelihood function (2.9) we find the gradient with respect to $P_{\boldsymbol{r}}$,$O_{\boldsymbol{r}}$ giving (2.10) here $\chi_{\boldsymbol{r}}$ is an auxiliary function given by (2.11) and * denotes the complex conjugate. The given equations are formulated for a Poisson noise model, the likelihood function might change if additional sources of noise are present (Thibault and Guizar-Sicairos, 2012). The minimum of (2.9) is found by implementing a conjugate gradient algorithm on (2.10), preconditioners can be useful in making the algorithm converge faster.

$$\begin{aligned}g_{P_{\boldsymbol{r}}} &= \frac{\partial \mathscr{L}}{\partial P_{\boldsymbol{r}}} = \sum_{j} O_{\boldsymbol{r}+\boldsymbol{r_j}} \chi^{*}_{j\boldsymbol{r}+\boldsymbol{r}_j}, \\ g_{O_{\boldsymbol{r}}} &= \frac{\partial \mathscr{L}}{\partial O_{\boldsymbol{r}}} = \sum_{j} P_{\boldsymbol{r}-\boldsymbol{r_j}} \chi^{*}_{j\boldsymbol{r}},\end{aligned} \tag{2.10}$$

$$\begin{aligned}\widetilde{\chi}_{j\boldsymbol{q}} &= \frac{\partial \mathscr{L}}{\partial I_{j\boldsymbol{q}}} \widetilde{\psi}_{j\boldsymbol{q}}, \\ &= w_{j\boldsymbol{q}} \left(1 - \frac{n_{j\boldsymbol{q}}}{I_{j\boldsymbol{q}}}\right) \widetilde{\psi}_{j\boldsymbol{q}}.\end{aligned} \tag{2.11}$$

2.3 Partial coherence of synchrotron sources and imaging with partially coherent probes

Fully coherent light sources are hard to find in reality. Though modern synchrotron sources generate x-rays with high coherence lengths, they can not be called ideal coherent sources (Thibault and Menzel, 2013; Singer and Vartanyants, 2014). It is often undesirable to have partial coherence, heavy constraints are imposed on experimental setup in order to make the probe as coherent as possible. This in turn leads to heavy filtering of the probe thus decreasing the usable flux by orders of magnitude. Apart from this, imperfect detection systems and inherent sample dynamics manifest into a behaviour equivalent to that of decoherence (Thibault and Menzel, 2013; Enders et al., 2014; Huang et al., 2015), therefore understanding coherence and its effect on ptychographic imaging becomes crucial.

Ptychographic measurement with a fully coherent probe can be represented as diffraction intensities collected at various points on the object where illumination function of the probe interacts with transmission function of the object in a simple multiplicative

manner (2.1). The same interaction can be thought of as object acting as an operator $\hat{O}_j = O_{\boldsymbol{r}-\boldsymbol{r_j}}$ acting on probe. To begin with, considering a fully coherent probe $P_{\boldsymbol{r}} = \langle \boldsymbol{r}|P\rangle$ giving rise to an exit wave $|\phi\rangle = \hat{O}_j|P\rangle$. The observed intensity then becomes (2.12) which is equivalent to (2.13).

$$I_{j\boldsymbol{q}} = |\langle \boldsymbol{q}|O_j|P\rangle|^2 . \tag{2.12}$$

Here Tr is the trace, $\mathscr{I}$ corresponds to an operator that is observable at coordinate $\mathbf{q}$ and related to measured intensity $I_{j\boldsymbol{q}}$ finally, $\rho = |P\rangle\langle P|$ is the density matrix of the pure incident photon state.

$$I_{j\boldsymbol{q}} = Tr\mathscr{I}_{j\boldsymbol{q}}\rho. \tag{2.13}$$

As we started off with an assumption that the probe is fully coherent, we represent it in pure state. Now the formulation of the ptychographic problem employing decoherent probe boils down to employing a probe with density matrix $\rho = \sum_{k=1}^{r}|P_k\rangle\langle P_k|$ where $\{|P_k\rangle\}$ are r orthogonal states of ρ and solving (2.12) which now becomes (2.14)

$$I_{j\boldsymbol{q}} = \sum_k |\langle \boldsymbol{q}|O_j|P_k\rangle|^2 . \tag{2.14}$$

Adapting the same formulation into existing algorithmic framework is straightforward as partially coherent probes can be expanded as sum of orthogonal coherent states (Thibault and Menzel, 2013; Singer and Vartanyants, 2014; Vartanyants and Singer, 2010).

2.4 Ptychotomography

A natural extension of two dimensional ptychographic imaging would be a three dimensional tomographic (Kak, 1985; Dierolf et al., 2010) reconstruction, exploiting high resolution 2D projections from the ptychography. (Holler et al., 2014) has previously showed that resolutions as good as 16 nm voxel size can be achieved using ptychotomography.For the moment ptychotomography is a blend of ptychography and conventional tomography, projections obtained from the ptychographic reconstruction at various angles are then processed through filtered back projection method (Diaz et al., 2012; Guizar-Sicairos et al., 2011) or algebraic reconstruction techniques (Guizar-Sicairos et al., 2015) to obtain three dimensional transmission maps of the sample involved. However, care should be taken so that the artefacts arising from ptychography do not corrupt the next step of tomography (Thibault and Guizar-Sicairos, 2012), hence corrections for phase ramp and phase un wrapping (Dierolf et al., 2010) are done to begin with. Apart from these the usual tomographic alignment issues remain to be corrected at the sinogram level (Kak, 1985; Allner, 2013). Once the corrections and

alignments are done the data is taken through tomographic reconstruction. Further details of ptychotomography will be discussed in the following chapters.

3 Methods

This chapter will be dedicated to explaining the methods involved in preparation and characterisation of nanostructures. Majority of the experiments were carried out at I13-coherence beamline Diamond Light Source (Pešić et al., 2013). Primarily two kinds of samples, nanoporous gold and limpet teeth were imaged using ptychographic imaging techniques, prior to ptychographic imaging the samples were characterised using alternative imaging techniques in order to gather complimentary evidence regarding the structure of the sample.

3.1 Nanoporous Gold

Nanoporous gold has spurred a lot of interest for its catalytic, conductive and mechanical properties. The material has found applications in catalysis, electronics and medicine (Seker et al., 2009). Apart from being a technologically important material it also serves as an ideal ptychographic sample given its ease of synthesis, strong scattering properties and tunability of nano features (Ding et al., 2004; Hakamada and Mabuchi, 2008) at the synthesis step.

Thin-film samples were prepared through a method similar to, what was mentioned in (Ding et al., 2004). 12 carat gold leaves (Gold leaf supplies, UK) were attached to kapton foils with holes, the kapton-gold leaf system was then made to float on Nitric acid(69% **sigma-aldrich**). The areas exposed to the nitric acid gets selectively dealloyed forming nanoporous gold fig 3.2. The sample was then transferred on to a TEM grid for further treatment and analysis. Dealloying produces nanostructures of uniform size with a narrow distribution of pore size. One way to introduce variations in the distribution of pore-size is to subject the dealloyed sample to annealing. The pore-size distribution depends on the time of annealing and the temperature at which annealing was carried out. Samples with various feature sizes at different length scales were prepared by exposing the typical gold leaf to acid for times ranging from 20 minutes to 7 days. Some of these samples were then subjected to annealing treatment at temperatures ranging from 200°C and 375°C for times ranging from 30 minutes to 2 hrs.

Figure 3.1: A. shows the floating gold foil and kapton system the orange areas are dealloyed nanoporous gold while white areas are unalloyed gold leaf. B shows mounted gold leaf on the TEM grids

Scanning electron microscopy analysis was done on the then prepared samples using Jeol, JSM-6610LV low vacuum scanning electron microscope. Some of the results are presented below.

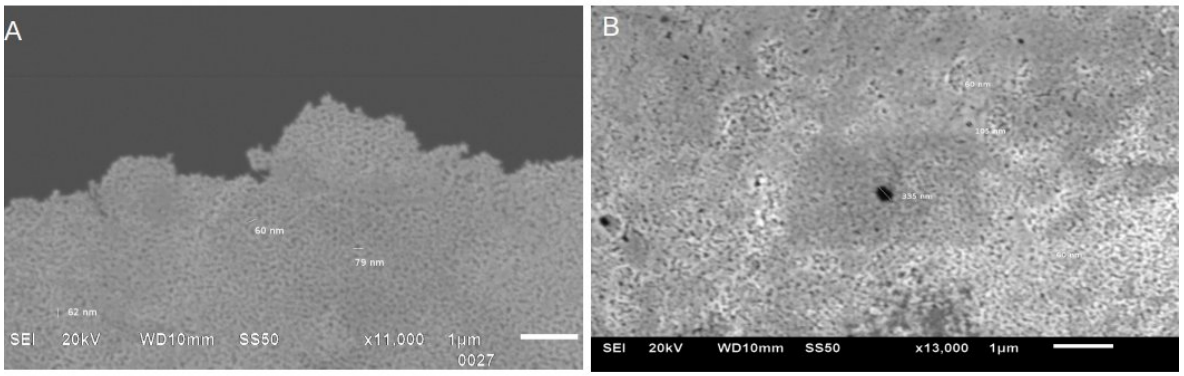

Figure 3.2: (A) SEM micrograph of NPG sample dealloyed for 38 hours with no further treatment. (B) SEM micrograph of NPG sample dealloyed for 20 minutes subjected to annealing for 150 minutes at 375°C.

3d nanoporous gold networks were prepared by etching small whiskers of 8 carat gold alloy obtained from chipping the 8 carat gold wire (Gold leaf supplies, UK) with a sharp scalpel. The whiskers were then etched using nitric acid (69% **sigma-aldrich**).

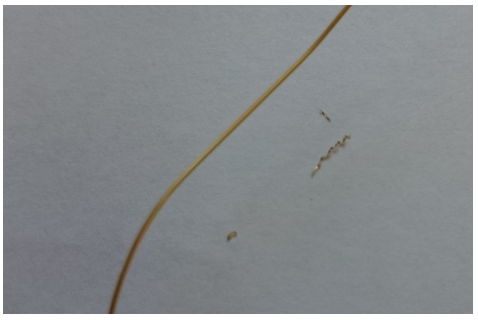

Figure 3.3: Gold whiskers obtained from a 8 carat gold wire.

From the experience gained through synthesis of nanoporous gold thin films, 3d gold nanoporous materials with feature sizes larger than 120 nm were prepared.

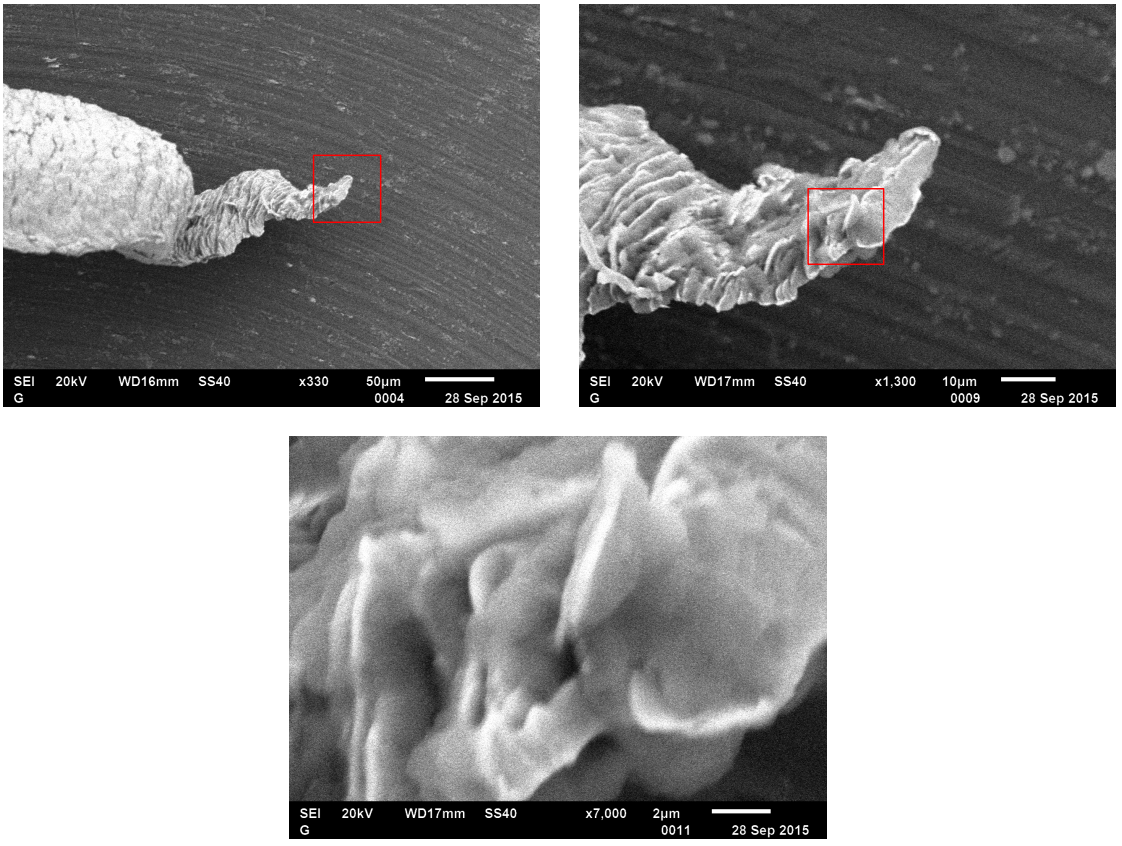

Figure 3.4: SEM micrograph of 8 carat NPG sample dealloyed for 48 hours and then subjected to annealing for 18 hours at 375°C.

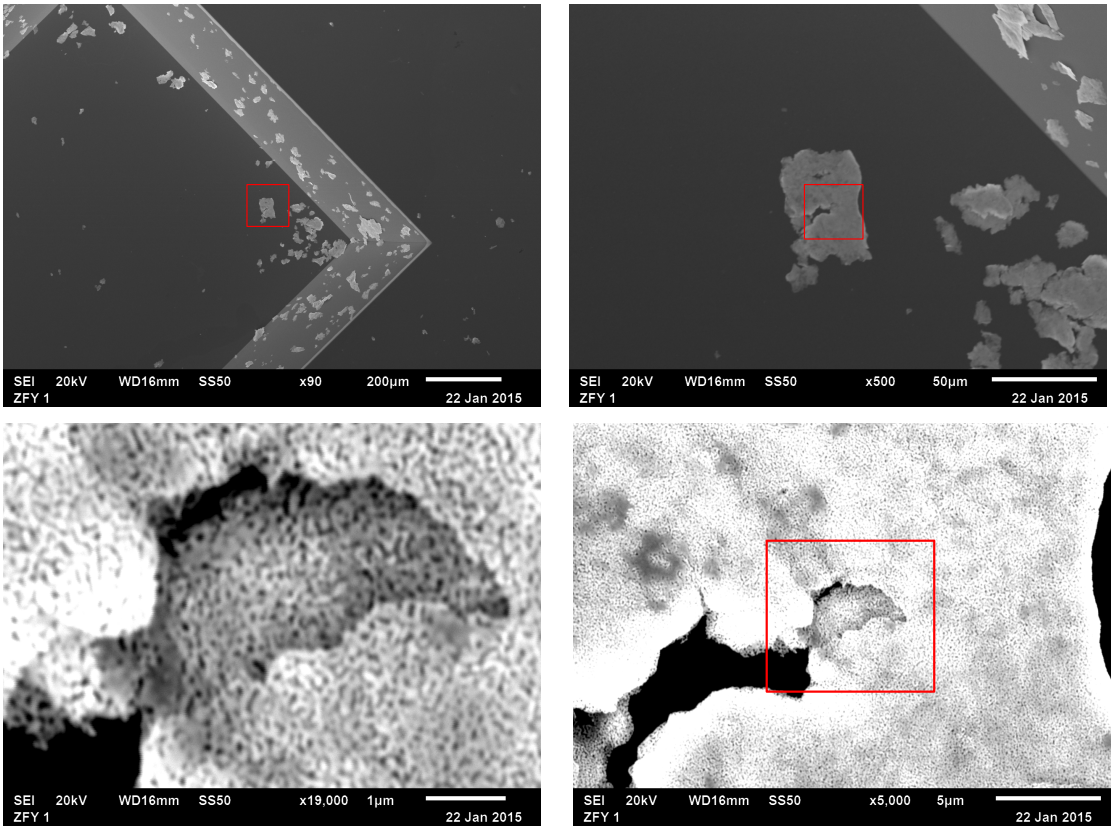

Figure 3.5: SEM micrograph of 8 carat NPG powder on SiN chips. Sample was dealloyed for 12 hours and then subjected to annealing for 3 hours at 375°C.

3.2 2D ptychographic imaging

2D ptychographic imaging can offer deeper insights into intricate two dimensional nanostructures, it has applications in areas such as microelectronics and microfluidics. We imaged samples ranging from weakly scattering electrode materials to bio nanocomposites like limpet teeth. Siemens star standard was used as a calibration sample for evaluating resolution and quality of obtained image at each step. Using this as a counter weight we fine-tuned various conditions of the beam to obtain optimum reconstructions. Presented below are some of the two dimensional reconstructions. Some of these form a subset of extensive three dimensional datasets. All the reconstructions shown below were reconstructed using ptychographic reconstruction code 'Ptycho' which was implimented and developed by Dr. Pierre Thibault and co-workers.

3.2.1 Diatoms

Diatoms are naturally occurring marine organisms made-up of porous silica structures. Radiation hardened and two dimensional these organisms act as ideal biological samples. Diatom samples were prepared from commercially available flea powder which was dispersed in ethanol and drop casted onto a kapton foil. The samples were imaged at an energy 9.7 keV, an exposure time of 2 seconds per frame and a detector to sample distance of 14.6 meters. Using the excalibur detector with a pixel size of 55 microns and 1796x2069 pixels wide. The obtainable real space pixel size in this geometry was 22 nm at the 1536x1536 cropping of the detector. The data was then processed through 150 difference map iterations and 900 maximum likelihood iterations employing single probe mode for reconstruction.

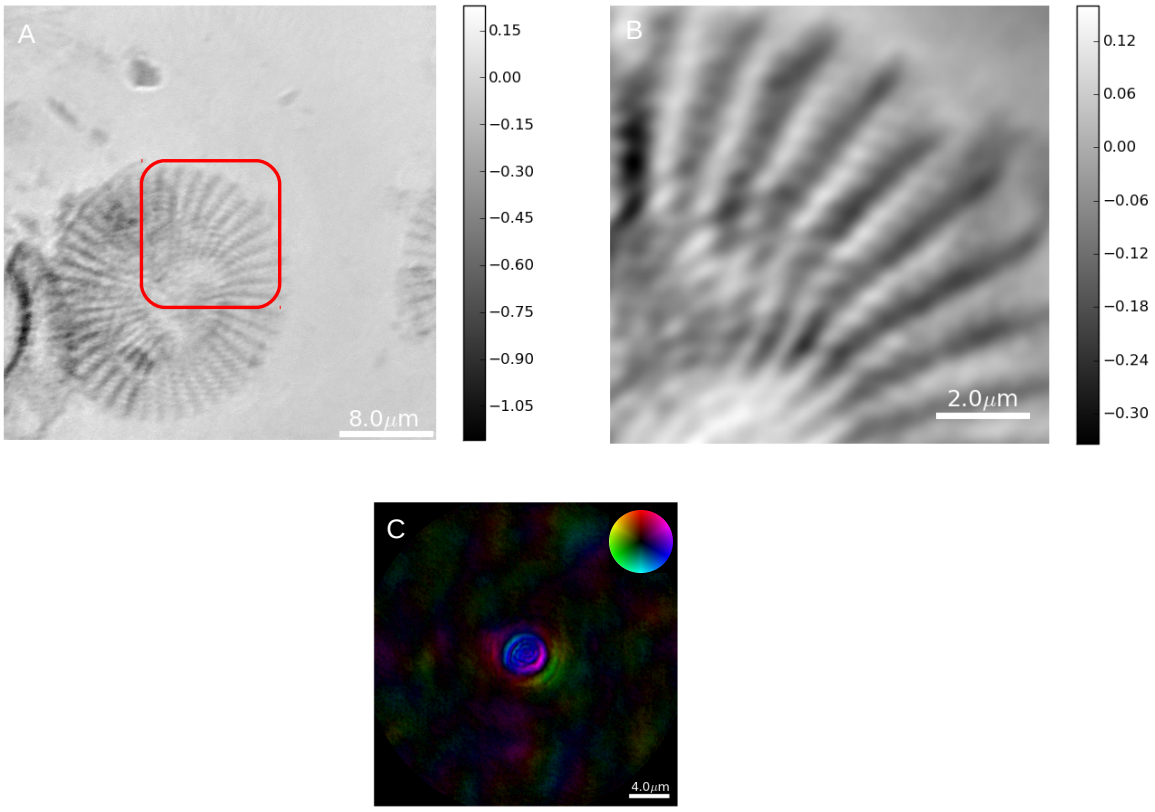

Figure 3.6: (A) Phase unwrapped image of diatom colony, (B) Enlarged ptychographic reconstruction of one diatom. (C) The associated probe. The gray scale shows the relative phase shift in radians.

3.2.2 Nanoporous Gold

Nanoporous gold 3D samples which were prepared as per section 3.1 were later characterised by ptychotomographic imaging at an energy 8.4 keV, an exposure time of .1 seconds per frame and a detector to sample distance of 6.7 meters. Using the merlin detector with a pixel size of 55 microns and 515x515 pixels wide. The obtainable real space pixel size in this geometry was 47 nm at the 512x512 cropping of the detector. The data was then processed through 150 difference map iterations and 300 maximum likelihood iterations employing 3 probe modes for reconstruction. Presented below in the fig 3.7 are the 2D reconstructions at $-90°$,$0°$,$90°$ respectively. 905 such projections were collected which are currently in the processing stage of ptychotomographic reconstructions.

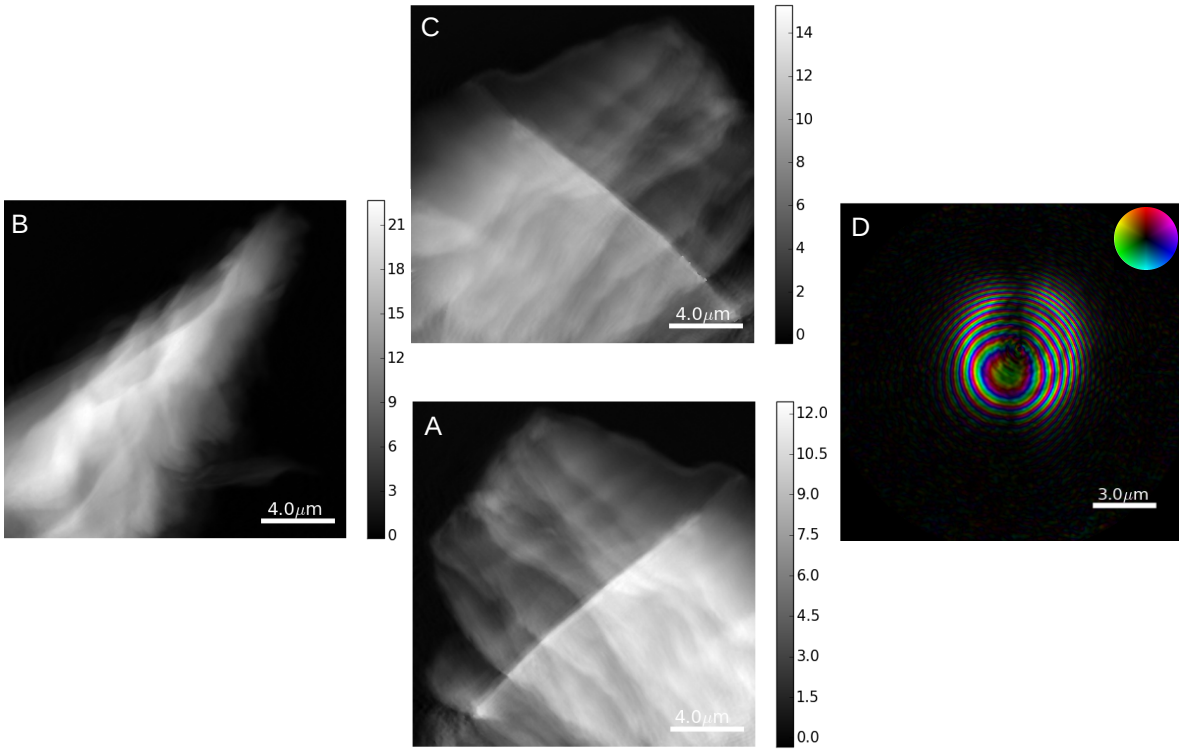

Figure 3.7: A,B,C,D. Phase unwrapped projections of nanoporous gold sample in 3.4 at $-90°$,$0°$,$90°$ degrees and the associated probe respectively. The gray scale shows the phase shift in radians.

Nanoporous gold 3D samples mounted on slat SiN substrate were characterised at energy 8.36 keV, an exposure time of .1 seconds per frame and a detector to sample distance of 6.4 meters. Using the merlin detector with a pixel size of 55 microns and 515x515 pixels wide. The obtainable real space pixel size in this geometry was 34 nm. The data was then processed through 300 difference map iterations and 500 maximum likelihood iterations employing 5 probe modes for reconstruction. This image forms a preliminary result for an elaborate limited angle Ptychotomography dataset that was collected on a similar sample, more of this will be discussed in the next chapter.

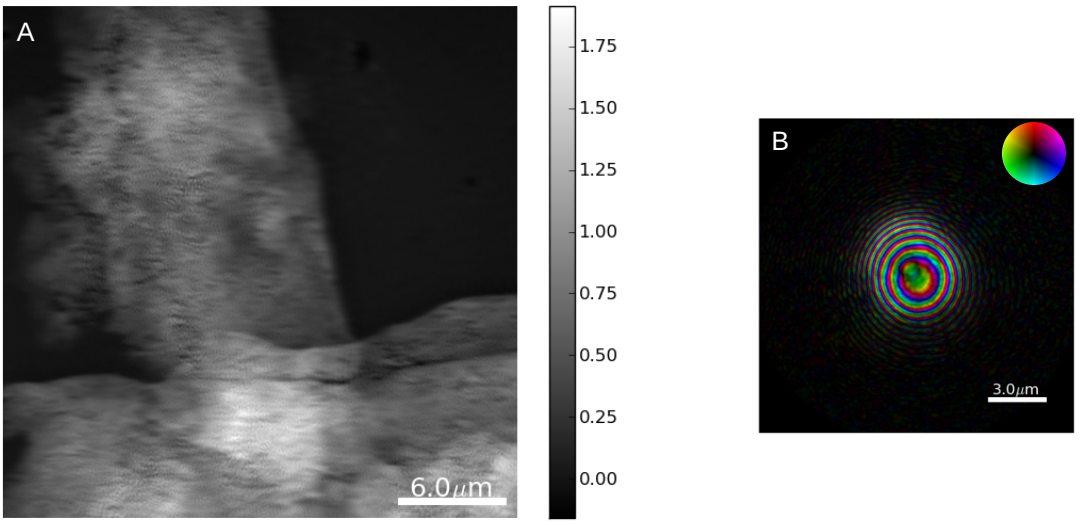

Figure 3.8: A,B. Phase unwrapped image of nanoporous gold sample similar to fig 3.5 and the associated probe. The gray scale shows the relative phase shift in radians.

3.2.3 Electrode materials

We have recently imaged high capacity Si anodes in collaboration with Dr. Anna M Wise of SLAC National Accelerator Laboratory, USA. The samples were characterised at an energy of 8.36 keV, an exposure time of .5 seconds per frame and a detector to sample distance of 6.4 meters. Using the merlin detector with a pixel size of 55 microns and 515x515 pixels wide. The obtainable real space pixel size in this geometry was 34 nm. The data was then processed through 300 difference map iterations and 500 maximum likelihood iterations employing 5 probe modes for reconstruction. The results presented below form preliminary results of a larger data set consisting limited angle tomography datasets of silicon/carbon electrodes power cycled at various stages.

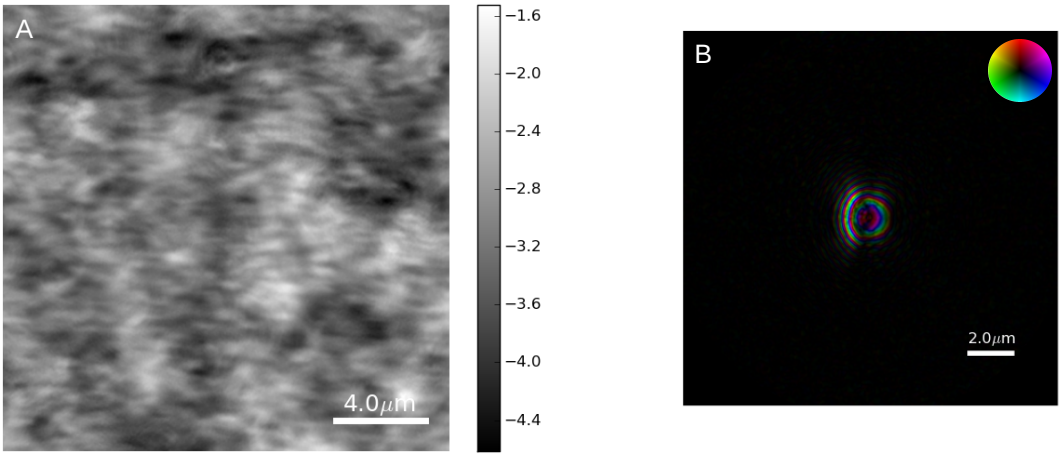

Figure 3.9: A is the phase unwrapped image of silicon carbon electrode material and B is the associated probe.The gray scale shows the relative phase shift in radians.

3.3 Ptychotomography of limpet teeth

Limpet teeth have recently emerged as the strongest naturally occurring bio material overtaking even the spider's silk (Barber et al., 2015). The limpet teeth achieve this by forming a complex bio-nanocomposite that blends high volume fraction nanofibre mineral crystals with soft protein rich areas. It is of immense interest to unlock the secrets behind the structure of this natural wonder, any information regarding the three dimensional arrangement of the soft and hard phases might throw interesting insights into the structure property relationship of limpet teeth. The ptychotomographic study was done in collaboration with Prof. Asa Barber of School of Engineering, University of Portsmouth.

Pluricuspid limpet teeth were imaged at an energy of 9.1 keV, an exposure time of 1 second per frame and a detector to sample distance of 6.2 meters. Using the excalibur detector with a pixel size of 55 microns and 1796x2069 pixels wide. The obtainable real space pixel size in this geometry was 35 nm at the 512x512 cropping of the detector. The data was then processed through 300 difference map iterations and 750 maximum likelihood iterations employing 3 probe modes for reconstruction. Presented below in

the fig 3.10 are the 2D reconstructions at −90°,0°,89° respectively. 180 such projections were collected and were then taken through ptychotomographic reconstruction process.

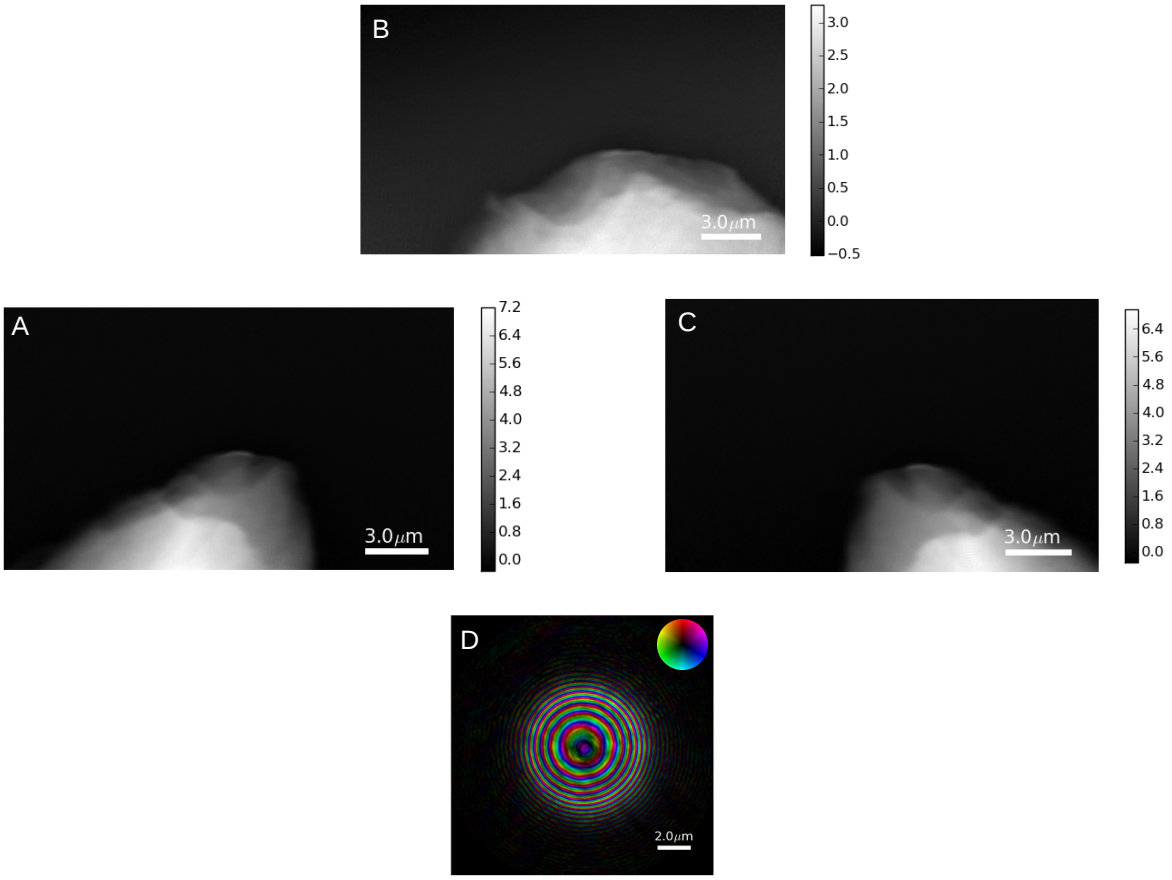

Figure 3.10: A,B,C,D. Phase unwrapped projections of nanoporous gold sample in 3.4 at −90°,0°,89° degrees and the associated probe respectively. The gray scale shows the phase shift in radians.

High resolution projections obtained from ptychographic reconstruction were firstly corrected for phase ramp and then the phase was unwrapped giving true projections fig 3.11 akin to what is obtained in conventional tomography. Sinograms were constructed by stacking up the individual rows of the angular projections fig 3.12. Normally the sinograms are then taken through alignment routines. Typical alignment techniques involve aligning centre of mass of each row of the sinogram or techniques like tomo-consistency (?). In this case however the as constructed sinograms were well aligned to begin with and therefore were not subjected any further alignment routines. The sinograms were subsequently taken through filtered back projection reconstruction to obtain three dimensional slices of the teeth sample fig 3.12.

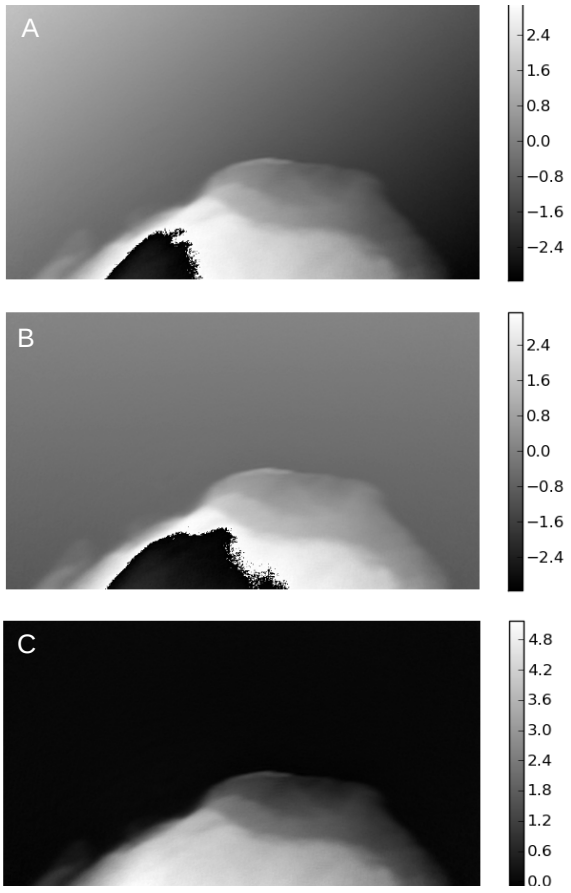

Figure 3.11: A,B,C illustrates the preprocessing steps of Ptychotomography. A is the raw projection, B is the projection corrected for phase ramp, C is the projection that has been phase unwrapped giving a true projection. The gray scale shows the relative phase shift in radians.

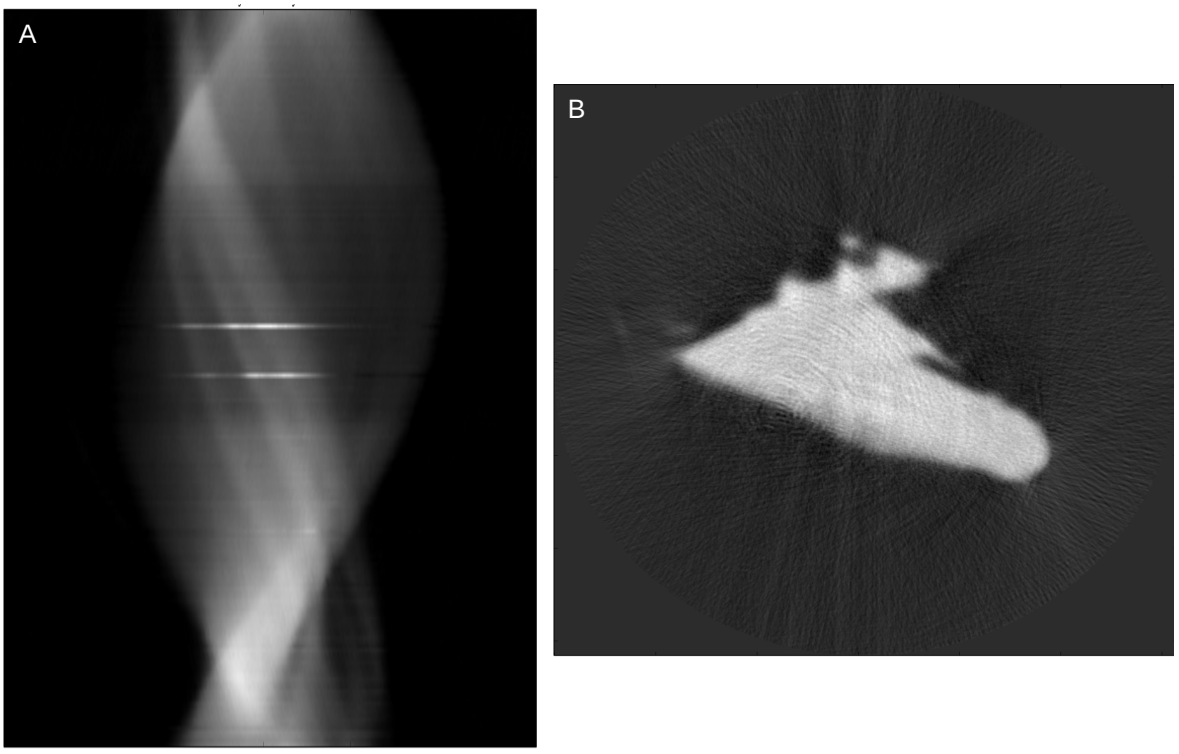

Figure 3.12: A is a typical sinogram of obtained from stacking rows of limpet teeth angular projections. B is the slice reconstructed using filtered back projection of the corresponding sinogram, HSV colorscheme was employed here as it gives a clearer picture compared to GRAY colorscheme.

The slices were then combined into a three dimensional matrix thus obtaining three dimensional transmission function of the limpet teeth. Presented below is an image of the cross section of the limpet teeth, we are unable to resolve the soft phase from the hard phase. We are currently fine tuning experimental parameters and further exploring ways to obtain higher resolution.

4 Future plans and prospects

This chapter will be dedicated to discussing the possible research avenues that could be explored in the future along with their repercussions on material characterisation and potential technological applications. Two important scientific cases, tomosynthesis and multiwavelength imaging will be discussed in the next sections. One handles the problem of missing angular projection data and its implications on the three dimensional reconstructions while the other might pave way towards novel material characterisation techniques.

4.1 Tomosynthesis

Limited angle tomography or tomosynthesis belongs to a subclass of computational tomography problems in which only partial angular data is available either due to sample limitations or experimental realities. Tomosynthesis has its roots in digital mammography, digital mammography is a one shot imaging technique producing an image of overlapping tissue which in-turn made detection of tumours hard. Tomosynthesis came as a breakthrough in which multiple, low dose projections were taken at a smaller angular range thus improving the probability of detecting the tumour along with reducing the radiation dose administered to the patient (Grant, 1972).

Limited angle tomographic problem might also arise due to the sample limitations especially in the case of a flat samples akin to that of fig 4.2. The consequence of missing angular data makes the three dimensional reconstruction problem extremely ill posed and the usual tomographic reconstruction procedure very unstable. Small errors in data measurement or extra noise may lead to large reconstruction errors, given the fact that any real experimental data is always corrupted by noise the problem becomes even more complicated. Demonstrated below is the limited angle tomographic reconstruction of the standard shepp-logan phantom. Added to the existing difficulties, further complications may arise purely from the ptychographic reconstruction procedure due to the fact that now the sample is similar to an extended plane rather than limited cylinder which was the case in the ptychography.

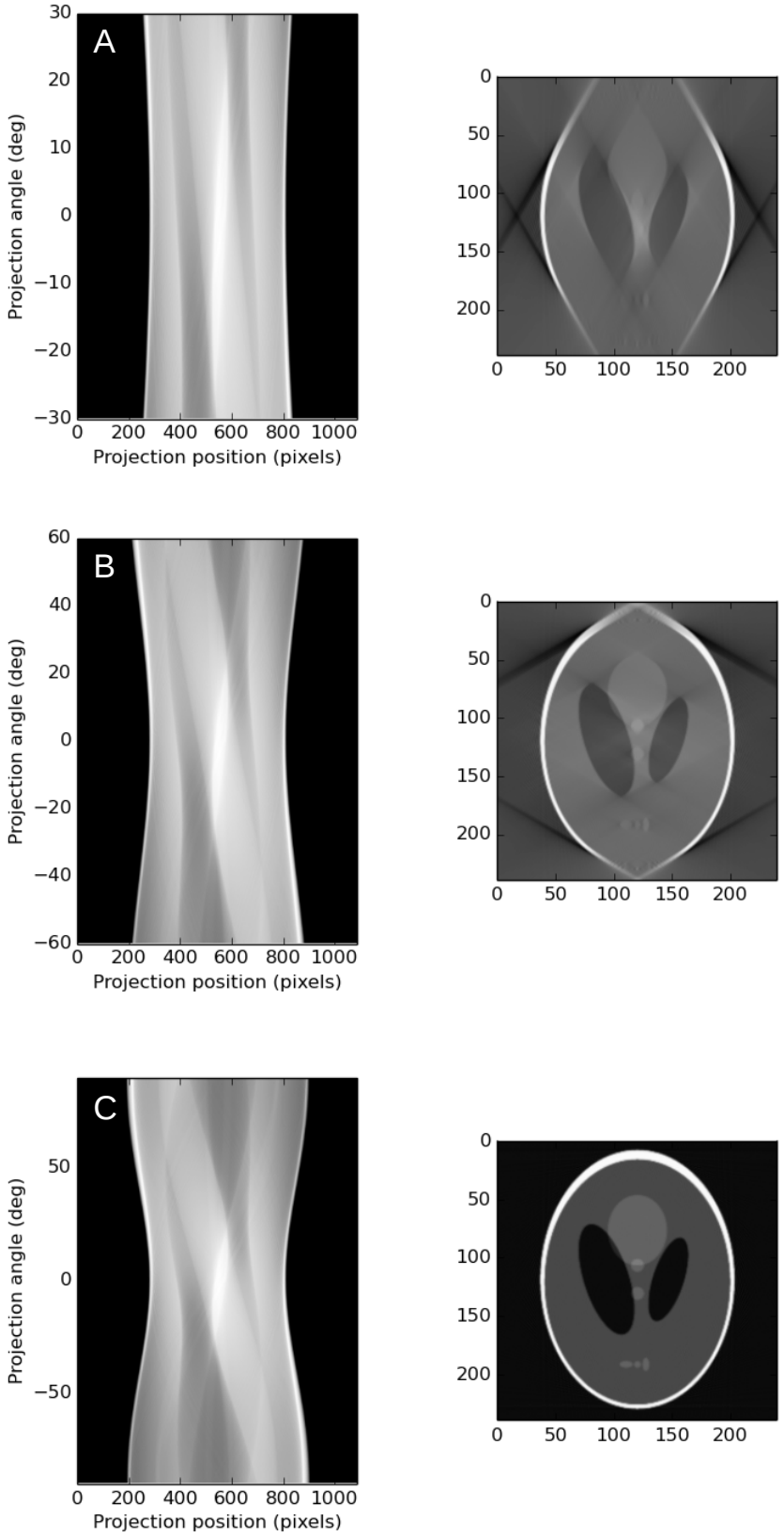

Figure 4.1: A,B,C. limited angle tomographic reconstruction of the standard shepp-logan phantom in the angular ranges $[-30°, 30°]$,$[-60°, 60°]$ and $[-90°, 90°]$ respectively.

Tackling the problem of limited angle tomography has its potential applications in diverse technological fields mainly in microelectronics. As per the Moore's law the electronic components are getting smaller and smaller thus making circuit design both challenging and complex. Tomosynthesis may find its applications in characterising planar, multilayered nano circuits that might become common than ever. With nanoelectronics facing challenges like circuit damage due to electromigration, tomosynthesis might play a key role in future micro/nanoelectronics.

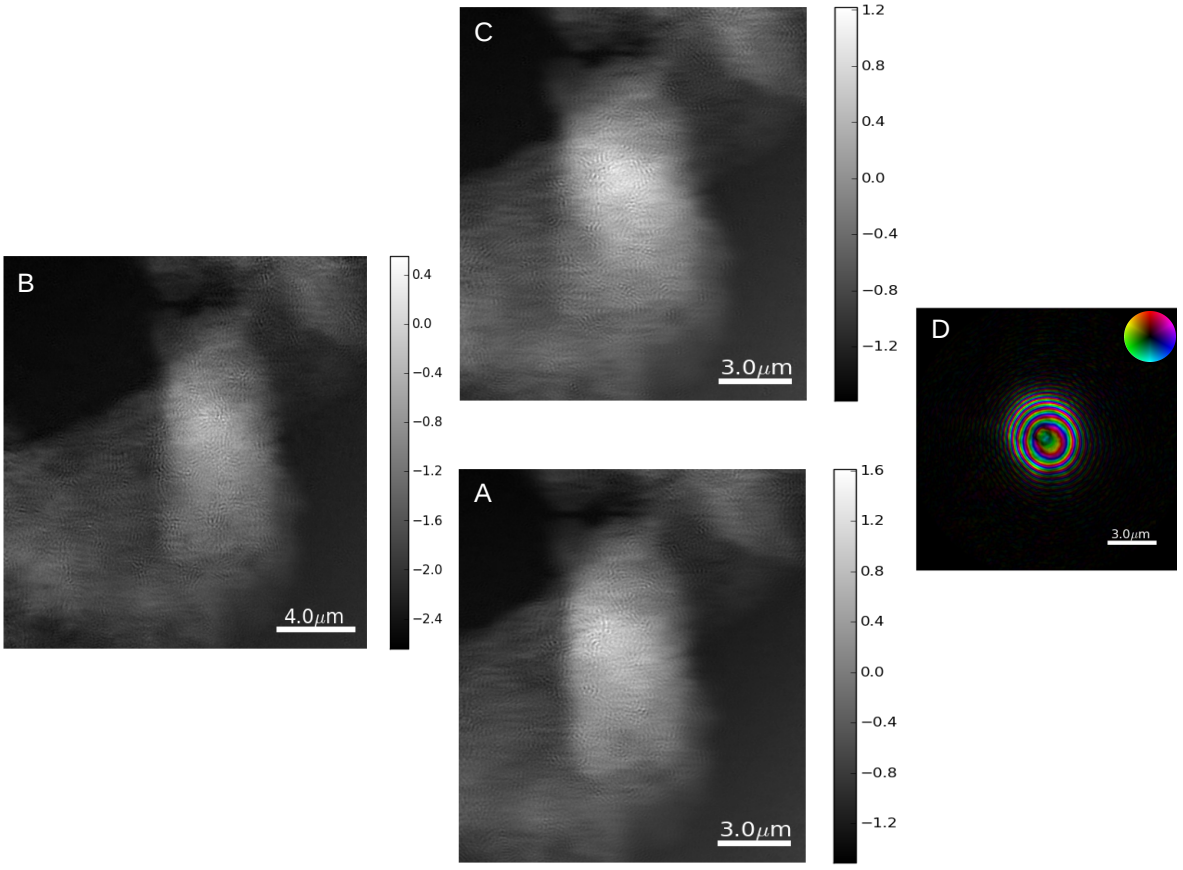

Figure 4.2: A,B,C,D. Phase unwrapped projections of nanoporous gold sample similar to fig 3.5 at $-20°$,$0°$,$20°$ degrees and the associated probe respectively. The gray scale shows the relative phase shift in radians.

Presented above are the two dimensional projections of a similar sample imaged under experimental conditions mentioned in section 3.2.2. 726 such projections were taken in the angular range of $[-60°, 60°]$ which are currently in the processing stage of limited angle ptychotomographic reconstructions.

4.2 Multiwavelength ptychographic imaging

X-rays can act as element specific contrast agents, (Elleaume et al., 2002) has previously demonstrated that imaging above and below absorption edges can give added contrast along with rough estimation of elemental distribution. Strictly speaking, accurate chemical information can only be obtained through spectroscopic imaging techniques (Ortega et al., 2007) but owing to the fact that the resolution of chemical information is dependent on probe size, it becomes practically impossible to image large volumes of data. Multiwavelength ptychography can therefore act as a bridge by obtaining rough estimate of elemental composition over large volumes of sample and then interesting areas can be further scanned using more accurate spectroscopic imaging methods.

We have recently imaged high capacity LiNi0.33Mn0.33Co0.33O2 cathodes in collaboration with Dr. Anna M Wise of SLAC National Accelerator Laboratory, USA. The samples were imaged at two wavelengths, above and below the nickel edge. The samples were imaged at energies of 8.32 and 8.36 keV with the same detector to sample distance of 6.4 meters. Using the merlin detector with a pixel size of 55 microns and 515x515 pixels wide. The obtainable real space pixel size in this geometry was 34 nm. The data was then processed through 300 difference map iterations and 500 maximum likelihood iterations.

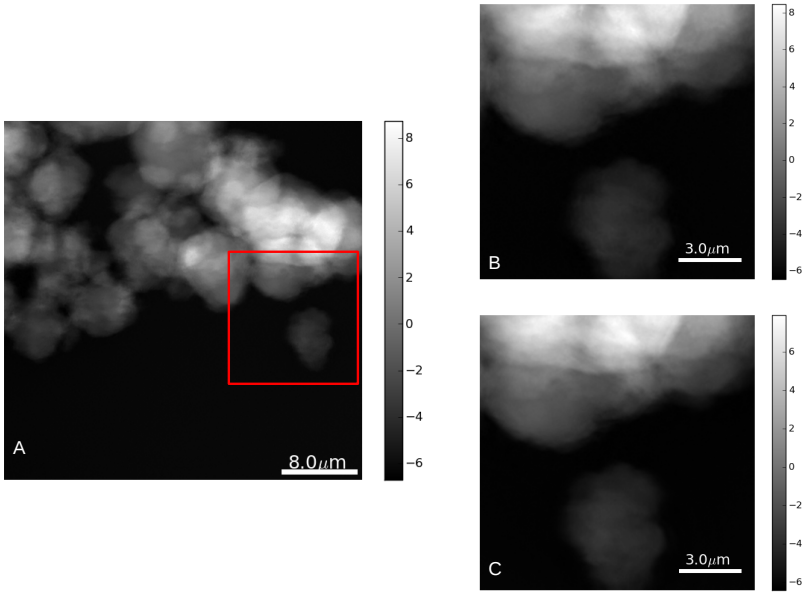

Figure 4.3: A,B,C. Phase unwrapped projections of LiNi0.33Mn0.33Co0.33O2 cathodes. A and B were imaged at 8.36 keV while C was imaged at 8.32 keV. The gray scale shows the relative phase shift in radians.

To begin with, the images were corrected for slight shifts due to the shift in the probe (fig 4.4). HSV colormap has been chosen over GRAY colormap owing to the clarity in representation of phase shift of the former over the later.

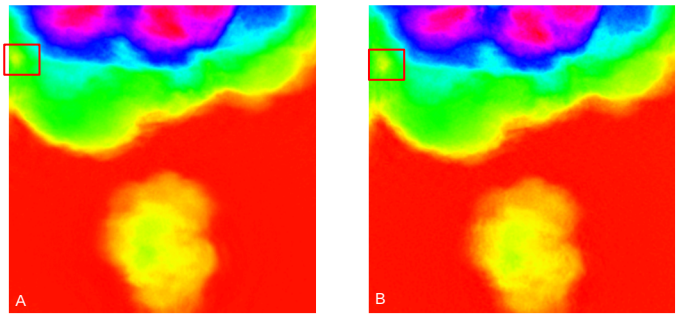

Figure 4.4: A and B are the images of same area taken at 8.32 and 8.36 respectively, the red square illustrates the slight shift of one image with respect to the other.

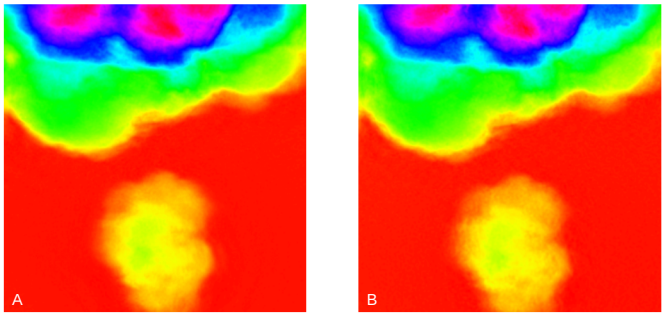

Figure 4.5: A and B are the images after the correction. The shifts between the images were calculated using cross correlation.

It might not be evident to begin with but once we subtract the image reconstructed at energy 8.32 keV (before the nickel edge) with the image reconstructed at energy 8.36 keV (after the edge) we obtain fig 4.6 showing the elemental contrast of nickel. We can selectively monitor the rough estimation of nickel distribution by considering only the positive variations and neglecting the negative variations in the subtracted image as illustrated by fig 4.7. This case study demonstrates the pros and cons of multiwavelength ptychographic imaging, while we were able to obtain rough estimate of nickel rich areas, we were unable to accurately map the chemical composition of the cathode material.

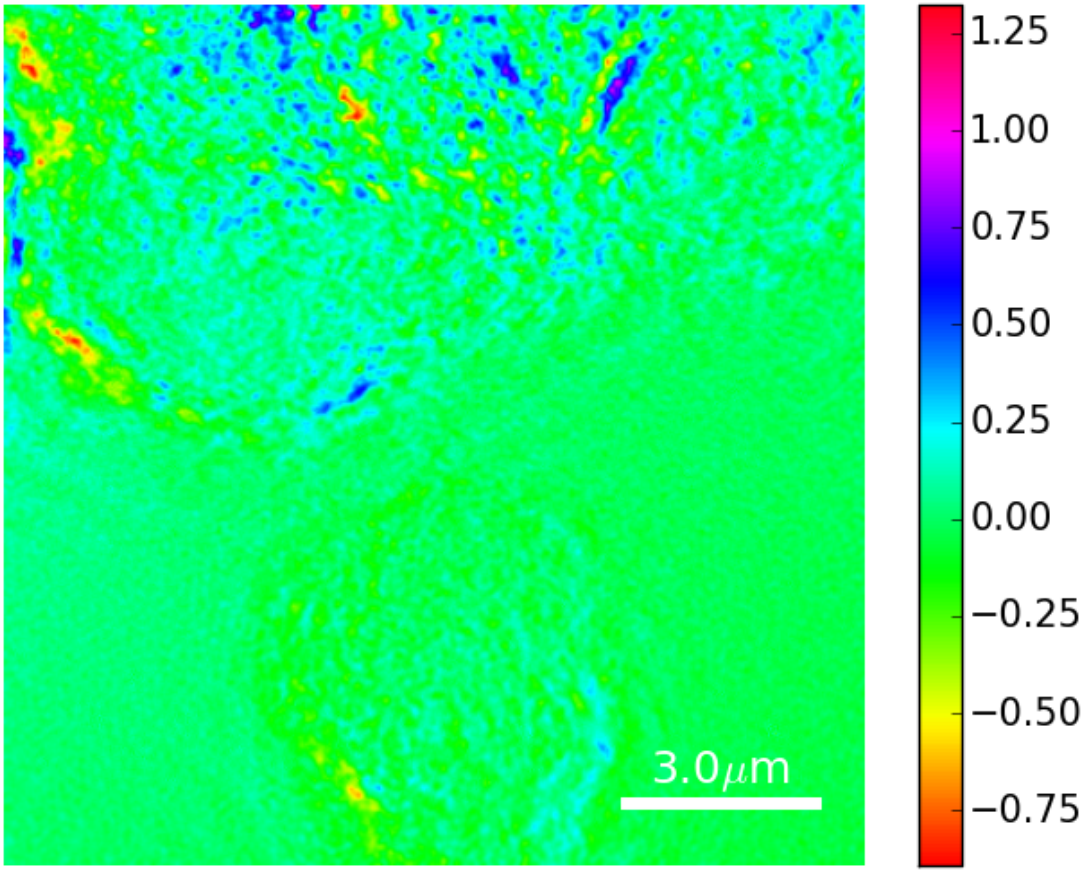

Figure 4.6: Difference in the images taken before and after the nickel edge.

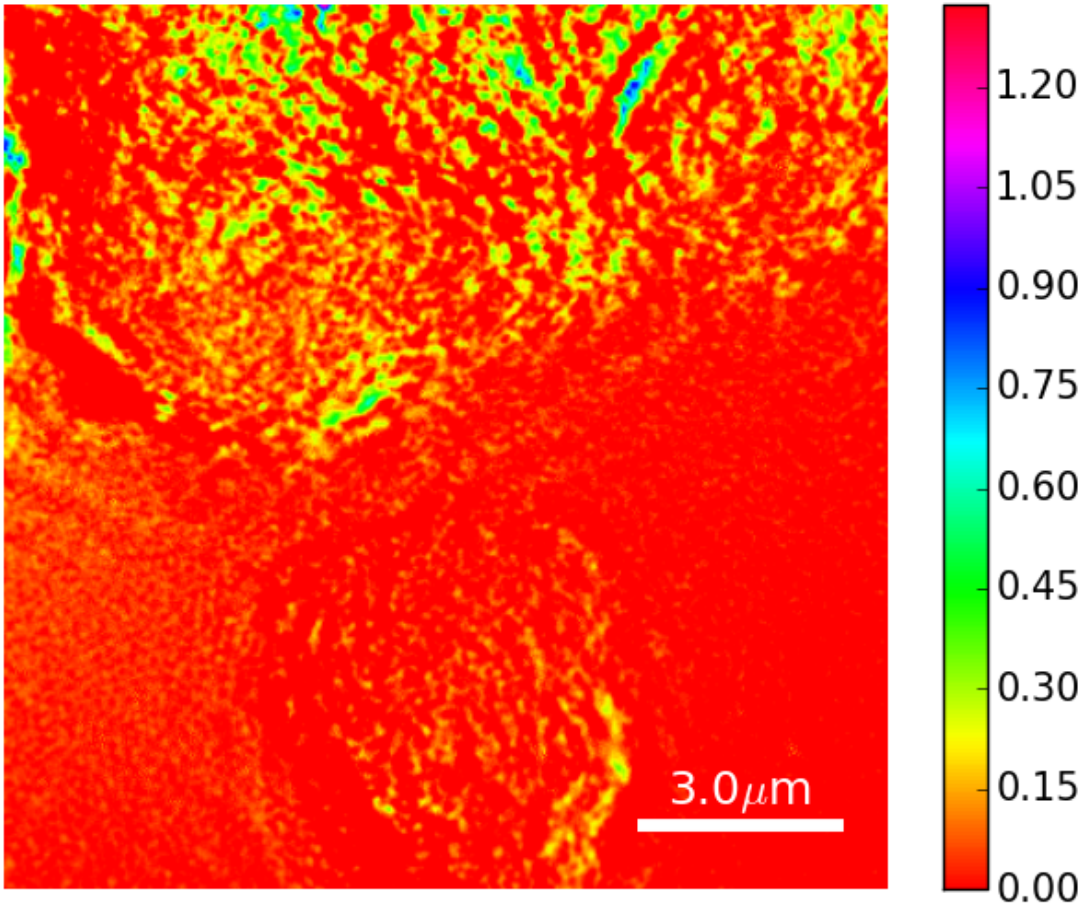

Figure 4.7: Rough estimate of nickel distribution in the sample.

Finally one can get the full picture by mapping the nickel rich areas on top of the ptychogram thus obtaining structural information with added information on elemental distribution.

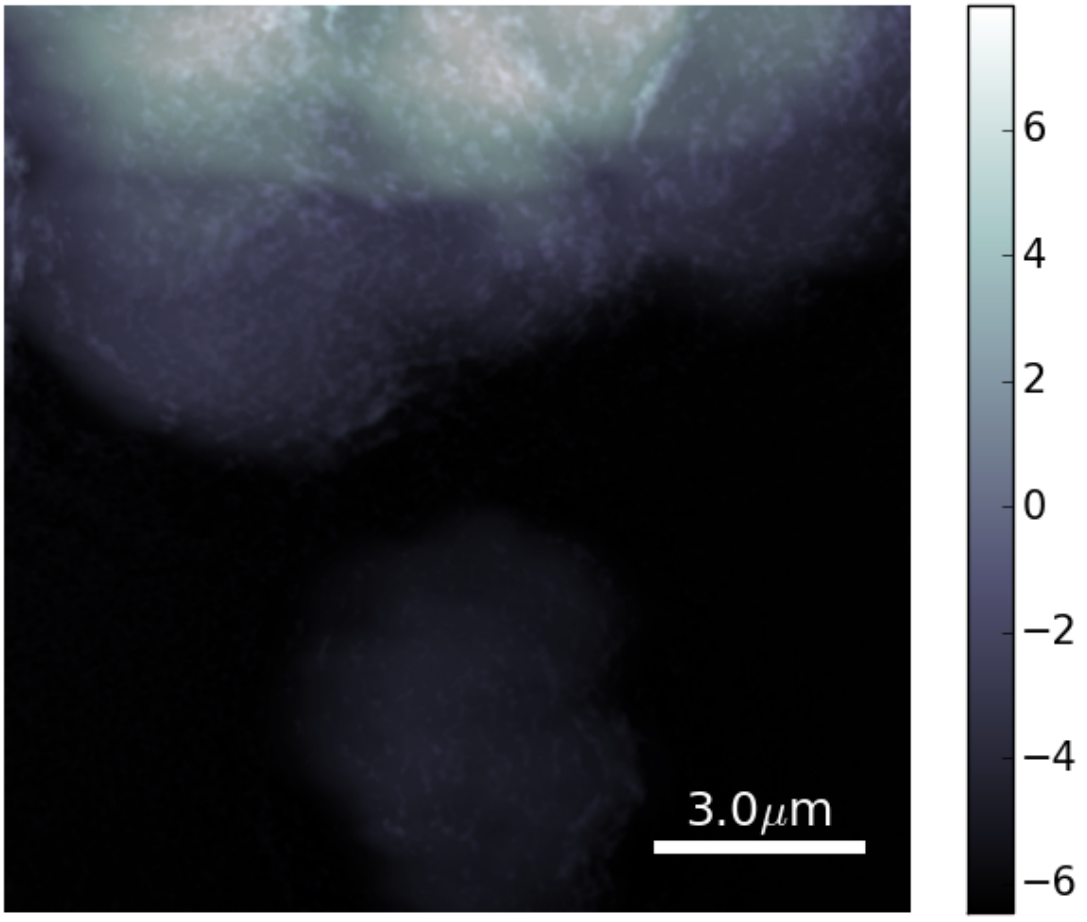

Figure 4.8: Shows the structural information (plotted in BONE colormap) with rough estimate of nickel distribution on top (plotted in GRAY colormap).

4.3 Conclusions

Ptychotomography has wide range of applications in materials science and emerging technologies. It can play a crucial role in solving complex scientific problems such as establishing structure property relationships in complex biologocal materials to determining failure mechanisms in microelectronics.

Limitations of sample preparation and fundamental nature of samples might pose challenges in three dimensional imaging, limited angle tomography is one such problem. Due to limited angular field of view, the three dimensional reconstruction problem be-

comes extremely ill posed. Minimising measurement errors and noise might be crucial in avoiding reconstruction errors. The future work will be aimed at understanding the limitations of ptychography applied to limited angle tomography problem.

Multiwavelength ptychographic imaging can offer element specific contrast. Though it is not as precise as spectroscopic imaging methods, owing to the fact that the spectroscopic imaging techniques are impractical when imaging large volumes makes multiwavelength ptychography an important bridge in obtaining approximate elemental distribution. Beam instabilities and long data acquisition times are the primary limitations of multiwavelength ptychography. Future work will be aimed at tackling some of these issues along with realising multiwavelength ptychotomography.

Bibliography

Allner, S. (2013). Local tomography alignment and bilateral filter post- processing for phase-contrast imaging,Dissertation.

Barber, A. H., Lu, D., Pugno, N. M., and Barber, A. H. (2015). Extreme strength observed in limpet teeth. *J. R. Soc. Interface*, 12(20141326):0–5.

Batey, D. J., Edo, T. B., Rau, C., Wagner, U., Pešić, Z. D., Waigh, T. A., and Rodenburg, J. M. (2014). Reciprocal-space up-sampling from real-space oversampling in x-ray ptychography. *Physical Review A - Atomic, Molecular, and Optical Physics*, 89(4):1–5.

Bø Fløystad, J., Skjønsfjell, E. T. B., Guizar-Sicairos, M., Høydalsvik, K., He, J., Andreasen, J. W., Zhang, Z., and Breiby, D. W. (2015). Quantitative 3D X-ray imaging of densification, delamination and fracture in a micro-composite under compression. *Advanced Engineering Materials*, 17(4):545–553.

Boll, K. (2013). Advanced Projection Alignment for Coherent X-ray nanoCT,Dissertation.

Chapman, H. N. (1997). Phase-Retrieval X-Ray Microscopy By Wigner-Distribution Deconvolution : Signal Processing. 11(925):67–80.

da Silva, J. C., Mader, K., Holler, M., Haberthür, D., Diaz, A., Guizar-Sicairos, M., Cheng, W.-C., Shu, Y., Raabe, J., Menzel, A., and van Bokhoven, J. A. (2015). Assessment of the 3 D Pore Structure and Individual Components of Preshaped Catalyst Bodies by X-Ray Imaging. *ChemCatChem*, 7(3):413–416.

Diaz, A., Trtik, P., Guizar-Sicairos, M., Menzel, A., Thibault, P., and Bunk, O. (2012). Quantitative x-ray phase nanotomography. *Physical Review B*, 85(2):1–4.

Dierolf, M., Menzel, A., Thibault, P., Schneider, P., Kewish, C. M., Wepf, R., Bunk, O., and Pfeiffer, F. (2010). Ptychographic X-ray computed tomography at the nanoscale. *Nature*, 467(7314):436–439.

Ding, Y., Kim, Y. J., and Erlebacher, J. (2004). Nanoporous gold leaf: "Ancient technology "/advanced material. *Advanced Materials*, 16(21):1897–1900.

Edo, T. B., Batey, D. J., Maiden, A. M., Rau, C., Wagner, U., Pešić, Z. D., Waigh, T. A., and Rodenburg, J. M. (2013). Sampling in x-ray ptychography. *Physical Review A - Atomic, Molecular, and Optical Physics*, 87(5):1–8.

Elleaume, H., Charvet, A. M., Corde, S., Estive, F., and Bas, J. F. L. (2002). Performance of computed tomography for contrast agent concentration measurements with monochromatic x-ray beams: comparison of k-edge versus temporal subtraction. *Physics in Medicine and Biology*, 47(18):3369.

Elser, V. (2002). Phase retrieval by iterated projections. *Journal of the Optical Society of America A*, 20(1):40–55.

Elser, V., Rankenburg, I., and Thibault, P. (2007). Searching with iterated maps. *Proceedings of the National Academy of Sciences of the United States of America*, 104(2):418–423.

Enders, B., Dierolf, M., Cloetens, P., Stockmar, M., Pfeiffer, F., and Thibault, P. (2014). Ptychography with broad-bandwidth radiation. *Applied Physics Letters*, 104(17):1–5.

Faulkner, H. M. L. and Rodenburg, J. M. (2004). Movable aperture lensless transmission microscopy: A novel phase retrieval algorithm. *Physical Review Letters*, 93(2):23901–23903.

Fienup, J. R. (1978). Reconstruction of an object from the modulus of its Fourier transform. *Optics letters*, 3(1):27–29.

Fienup, J. R. (1982). Phase retrieval algorithms: a comparison. *Applied Optics*, 21(15):2758–2769.

Fienup, J. R. (1997). Invariant error metrics for image reconstruction. *Applied optics*, 36(32):8352–8357.

Gerchberg, R W and Saxton, W O (1972). Quantitative 3D X-ray imaging of densification, delamination and fracture in a micro-composite under compression. *Optik*, 35(35):2–5.

Grant, D. G. (1972). Radiographic Imaging Technique. (1):20–28.

Guizar-Sicairos, M., Boon, J. J., Mader, K., Diaz, A., Menzel, A., and Bunk, O. (2015). Quantitative interior x-ray nanotomography by a hybrid imaging technique. *Optica*, 2(3):259–266.

Guizar-Sicairos, M., Diaz, A., Holler, M., Lucas, M. S., Menzel, A., Wepf, R. a., and Bunk, O. (2011). Phase tomography from x-ray coherent diffractive imaging projections. *Optics Express*, 19(22):21345.

Guizar-Sicairos, M., Holler, M., Diaz, A., Vila-Comamala, J., Bunk, O., and Menzel, A. (2012). Role of the illumination spatial-frequency spectrum for ptychography. *Physical Review B - Condensed Matter and Materials Physics*, 86(10):1–4.

Hakamada, M. and Mabuchi, M. (2008). Microstructural evolution in nanoporous gold by thermal and acid treatments. *Materials Letters*, 62(3):483–486.

Holler, M., Diaz, a., Guizar-Sicairos, M., Karvinen, P., Färm, E., Härkönen, E., Ritala, M., Menzel, a., Raabe, J., and Bunk, O. (2014). X-ray ptychographic computed tomography at 16 nm isotropic 3D resolution. *Scientific reports*, 4:3857.

Horowitz, P., Howell, J. A., Series, N., and Nov, N. (1972). A Scanning X-Ray Microscope Using Synchrotron Radiation . 178(4061):608–611.

Huang, X., Lauer, K., Clark, J. N., Xu, W., Nazaretski, E., Harder, R., Robinson, I. K., and Chu, Y. S. (2015). Fly-scan ptychography. *Scientific Reports*, 5:9074.

Kak, A. C. (1985). Tomographic imaging with diffracting and non-diffracting sources. *in Array Signal Processing,*.

Kewish, C. M., Guizar-Sicairos, M., Liu, C., Qian, J., Shi, B., Benson, C., Khounsary, A. M., Vila-Comamala, J., Bunk, O., Fienup, J. R., Macrander, A. T., and Assoufid, L. (2010a). Reconstruction of an astigmatic hard X-ray beam and alignment of K-B mirrors from ptychographic coherent diffraction data. *Optics express*, 18(22):23420–23427.

Kewish, C. M., Thibault, P., Dierolf, M., Bunk, O., Menzel, A., Vila-Comamala, J., Jefimovs, K., and Pfeiffer, F. (2010b). Ptychographic characterization of the wavefield in the focus of reflective hard X-ray optics. *Ultramicroscopy*, 110(4):325–329.

Luke, D. R. (2005). Relaxed averaged alternating reflections for diffraction imaging. 21:37–50.

McCallum, B. C. and Rodenburg, J. M. (1992). Two-dimensional demonstration of Wigner phase-retrieval microscopy in the STEM configuration. *Ultramicroscopy*, 45(3-4):371–380.

Mezouar, M., Crichton, W. A., Bauchau, S., Thurel, F., Witsch, H., Torrecillas, F., Blattmann, G., Marion, P., Dabin, Y., Chavanne, J., Hignette, O., Morawe, C., and Borel, C. (2005). Development of a new state-of-the-art beamline optimized for monochromatic single-crystal and powder X-ray diffraction under extreme conditions at the ESRF. *Journal of Synchrotron Radiation*, 12(5):659–664.

Miao, J., Charalambous, P., Kirz, J., and Sayre, D. (1999). Extending the methodology of X-ray crystallography to allow imaging of micrometre-sized non-crystalline specimens. *Nature*, 400(6742):342–344.

Ortega, R., Cloetens, P., Devès, G., Carmona, A., and Bohic, S. (2007). Iron storage within dopamine neurovesicles revealed by chemical nano-imaging. *PLoS ONE*, 2(9).

Pešić, Z. D., Fanis, a. D., Wagner, U., and Rau, C. (2013). Experimental stations at I13 beamline at Diamond Light Source. *Journal of Physics: Conference Series*, 425(18):182003.

Pfeifer, M. a., Williams, G. J., Vartanyants, I. a., Harder, R., and Robinson, I. K. (2006). Three-dimensional mapping of a deformation field inside a nanocrystal. *Nature*, 442(7098):63–66.

Rodenburg, J. M., Hurst, A. C., Cullis, A. G., Dobson, B. R., Pfeiffer, F., Bunk, O., David, C., Jefimovs, K., and Johnson, I. (2007). Hard-X-ray lensless imaging of extended objects. *Physical Review Letters*, 98(3):1–4.

Sayre, D. (1952). Some implications of a theorem due to Shannon. *Acta Crystallographica*, 5(6):843.

Schenk, T., Thi, H. N., Gastaldi, J., Reinhart, G., Cristiglio, V., Mangelinck-NoÃńl, N., Klein, H., HÃďrtwig, J., Grushko, B., Billia, B., and Baruchel, J. (2005). Application of synchrotron x-ray imaging to the study of directional solidification of aluminium-based alloys. *Journal of Crystal Growth*, 275(1âĂŞ2):201 – 208.

Seker, E., Reed, M. L., and Begley, M. R. (2009). Nanoporous gold: Fabrication, characterization, and applications. *Materials*, 2(4):2188–2215.

Singer, A. and Vartanyants, I. A. (2014). Coherence properties of focused X-ray beams at high-brilliance synchrotron sources. *Journal of Synchrotron Radiation*, 21(1):5–15.

Thibault, P. (2007). Algorithmic Methods in Diffraction Microscopy,Dissertation.

Thibault, P. (2008). High-Resolution Scanning X-ray Diffraction Microscopy. *Science*, 379(July):379–383.

Thibault, P., Dierolf, M., Bunk, O., Menzel, A., and Pfeiffer, F. (2009). Probe retrieval in ptychographic coherent diffractive imaging. *Ultramicroscopy*, 109(4):338–343.

Thibault, P. and Guizar-Sicairos, M. (2012). Maximum-likelihood refinement for coherent diffractive imaging. *New Journal of Physics*, 14:1–20.

Thibault, P. and Menzel, A. (2013). Reconstructing state mixtures from diffraction measurements supplement. *Nature*, 494(7435):68–71.

Thibault, P. and Rankenburg, I. C. (2007). Optical diffraction microscopy in a teaching laboratory. *American Journal of Physics*, 75(9):827.

van der Veen, J. F. (2004). Coherent x-ray scattering. *Journal of physics. Condensed matter*, 16(28):5003–5030.

Vartanyants, I. A. and Singer, A. (2010). Coherence properties of hard x-ray synchrotron sources and x-ray free-electron lasers. *New Journal of Physics*, 12:1–23.

Walker, S. M., Schwyn, D. A., Mokso, R., Wicklein, M., M??ller, T., Doube, M., Stampanoni, M., Krapp, H. G., and Taylor, G. K. (2014). In Vivo Time-Resolved Microtomography Reveals the Mechanics of the Blowfly Flight Motor. *PLoS Biology*, 12(3).

Yang, C., Qian, J., Schirotzek, a., Maia, F., and Marchesini, S. (2011). Iterative Algorithms for Ptychographic Phase Retrieval. *Contemporary Mathematics*, 0:32.

Acknowledgements

First and foremost I would like to express my deepest gratitude to my supervisor **Dr. Pierre Thibault** for his constant supervision and support in compiling this work. I cannot thank him enough for his patience in putting up with me. I will always be thankful to him for teaching me and guiding me.

I am grateful to **Dr. Christoph Rau** for his support and help. I will always be thankful to him for letting me use the facilities at Diamond Light Source.

I would like to thank my colleagues Stefanos Horst-Chalkidis, Simone Sala and Marie-Christine Zdora for their support,guidance and help.

Further thanks go to Dr. Ulrich Wagner, Dr. Aaron Parsons, Dr. Andrew Bodey, Mirna Saliba, Simon Logan, Dr. Kaz Wanelik, for their co-operation and help.

Finally, I am deeply grateful to my parents, my siblings Siri, Teja and Tarun, my family and my friends for their consistent love, support and encouragement.